Asian Journal of Chemistry; Vol. 38, No. 2 (2026), 425-433

ASIAN JOURNAL OF CHEMISTRY

https://doi.org/10.14233/ajchem.2026.34808

ZnO Thin Films Synthesized by Ultra Spray Pyrolysis: Structural Characterization, Gas Sensing Behaviour and Antimicrobial Activity

SUPRIYA SHUKLA[1], SURAJ SALUNKHE[1], VAISHALI RAUT[1], SAURABH MOHITE[1],
KIRAN KUMAR SHARMA[2] and SHARDA GADALE[1,*]

[1]Department of Chemistry, Yashwantrao Mohite College of Arts, Science and Commerce, Pune-411038, India
[2]Department of Chemistry, School of Nanoscience and Biotechnology, Shivaji University, Kolhapur-416004, India

*Corresponding author: E-mail: dagade@rediffmail.com

Received: 15 September 2025 *Accepted*: 5 January 2026 *Published online*: 31 January 2026 AJC-22260

In this work, ZnO thin films were prepared using the ultra-spray pyrolysis technique at 300 ºC, employing precursor (zinc acetate) molarities of 0.3 M, 0.4 M, 0.5 M and 0.6 M. The structural, morphological, optical and compositional properties of the films were systematically investigated using X-ray diffraction (XRD), UV-visible spectroscopy, energy-dispersive X-ray analysis (EDX), field-emission scanning electron microscopy (FESEM), X-ray photoelectron spectroscopy (XPS), and atomic force microscopy (AFM). XRD analysis confirmed the formation of polycrystalline ZnO films with a preferential orientation along the (101) crystallographic plane. AFM measurements revealed that the films deposited at higher precursor concentrations exhibited reduced thickness and improved surface smooth-ness, with a minimum roughness value of 8.94 nm. Optical studies showed that the band gap energy of the ZnO thin films varied between 3.0 and 3.4 eV, depending on the molarity. FESEM images indicated the presence of uniformly distributed nanometric grains with a hexagonal morphology across all samples. Gas-sensing devices fabricated from the ZnO films demonstrated effective detection of NO_2 gas, with the 0.6 M film exhibiting the highest response of approximately 43.6 toward 40 ppm NO_2 at an operating temperature of 463 K. The enhanced sensing performance is attributed to surface defects and oxygen vacancies induced by Zn^{2+}-related non-stoichiometry, which facilitate charge transfer during gas adsorption and promote the sensing mechanism. Moreover, prepared ZnO thin films exhibited significant antibacterial activity against *Staphylococcus aureus*, *Escherichia coli*, *Pseudomonas aeruginosa* and *Bacillus subtilis*, attributed to reactive oxygen species generation and Zn^{2+}-mediated cell wall disruption, with the 0.4 M film showing the highest efficacy.

Keywords: Ultra spray pyrolysis, ZnO Thin films, Optical band gap, Gas sensor.

INTRODUCTION

Environmental pollution remains a critical global challenge, motivating the development of semiconductor-based gas sensors for air-quality monitoring. Among harmful pollutants, nitrogen dioxide (NO_2) is of particular concern due to its role in ground-level ozone formation and its adverse health effects. Even low-level exposure (~3 ppm) can irritate the respiratory system, while higher or prolonged exposure may cause severe lung impairment and increased mortality risk [1]. Consequently, various gas-monitoring materials, including conducting polymer composites, metal oxide semiconductors and metal oxide-polymer hybrids, have been developed for NO_2 detection [2,3]. Among these, metal oxide semiconductor sensors have attracted particular interest due to their superior long-term stability [4]. Their small size and straightforward sensing mechanism facilitate their integration and downsizing into electronic circuits.

Inorganic antibacterial materials have gained considerable attention due to their effectiveness at low concentrations and their superior stability under harsh conditions such as high temperature and pressure [5-8]. Among these materials, zinc oxide (ZnO) stands out due to its wide band gap, chemical stability, non-toxicity, and cost-effectiveness. ZnO exists in three crystalline phases rock salt, zinc blende and wurtzite, of which the hexagonal wurtzite structure is thermodynamically stable at ambient conditions, with each Zn atom tetrahedrally coordinated to four oxygen atoms [9,10]. This crystal structure supports efficient charge transport and defect formation, which are crucial for sensing and antimicrobial applications.

ZnO thin films and nanostructures have been synthesized using various techniques, including spray pyrolysis [11-13],

---

co-precipitation [14,15], ball milling [16,17], sol-gel processing [18,19] and microwave-assisted methods [20,21]. Several studies have reported strong antibacterial activity of ZnO nanostructures prepared through these approaches [22-25], attributed to reactive oxygen species generation, surface defects, and Zn^{2+} ion release. Owing to their unique physico-chemical properties and ease of fabrication, ZnO-based materials have also found applications in gas sensing [26,27], biosensors [28,29], biomedicine [30,31] and catalysis [32-34].

Among the available deposition methods, ultra-spray pyrolysis offers distinct advantages for fabricating ZnO thin films, including simplicity, scalability and precise control over film morphology and defect density. These parameters critically influence gas-sensing behaviour, particularly toward oxidizing gases such as NO_2, as well as antimicrobial performance. In this work, ZnO thin films synthesized by ultra-spray pyrolysis at different precursor concentrations are systematically investigated to correlate their structural, optical, gas-sensing, and antibacterial properties, highlighting their potential for environmental monitoring and antimicrobial applications.

EXPERIMENTAL

Synthesis: ZnO thin films were fabricated on glass substrates by ultra-spray pyrolysis using a Sonotech TOP 5300 system. Zinc acetate tetrahydrate (99.3% purity) was employed as the precursor. The solution was atomized ultrasonically and delivered to the heated substrate using dried compressed air, where thermal decomposition led to ZnO film growth. The deposition was carried out with a nozzle-substrate distance of 20 cm, carrier gas pressure of 7 N cm^{-2}, solution flow rate of 0.38 mL s^{-1} and total spray volume of 50 mL. These optimized parameters yielded homogeneous and well-adhered ZnO thin films. Four different thin films with varying concentrations of 0.3 M, 0.4 M, 0.5 M and 0.6 M of precursor were prepared by following above mentioned procedure.

Characterization: The structural properties of the prepared ZnO thin films were analyzed using X-ray diffraction (XRD) recorded on a Rigaku MiniFlex 300 diffractometer with Cu$K\alpha$ radiation (λ = 1.5406 Å). Optical absorption spectra were measured at room temperature using a JASCO V-630 UV-visible spectrophotometer, and the optical band gap was estimated from Tauc plots. Surface morphology and grain structure were examined by field-emission scanning electron microscopy (FESEM) using a JEOL JSM-7600F instrument. Surface chemical composition and elemental states were investigated by X-ray photoelectron spectroscopy (XPS) employing a PHI 5000 VersaProbe III spectrometer with Al$K\alpha$ radiation. Surface topography and roughness were evaluated using atomic force microscopy (AFM) on a Bruker Dimension Icon system operating in tapping mode.

Gas-sensing characteristics were measured using a custom built airtight stainless-steel test chamber. ZnO thin films with dimensions of 1 cm × 2 cm were mounted inside the chamber, and sensor performance was evaluated by monitoring resistance changes upon exposure to the target gas under controlled conditions.

Antibacterial activity: The antibacterial activity of the test samples was evaluated using the agar-well diffusion method. Fresh cultures of *Bacillus subtilis*, *Escherichia coli*, *Pseudomonas aeruginosa* and *Staphylococcus aureus* were grown in nutrient broth at 37 ºC for 24 h prior to analysis. Nutrient agar plates were prepared and uniformly inoculated with 100 µL of each bacterial suspension using a sterile spreader to obtain a confluent lawn. After inoculation, wells of 6-8 mm diameter were aseptically punched into the agar using a sterile cork-borer. The test material was dissolved in DMSO to obtain a stock concentration of 10 mg mL^{-1} and 50 µL of this solution was carefully dispensed into each well. Streptomycin (Abbott Healthcare Pvt. Ltd.) was used as the standard antibacterial agent for comparison, while DMSO served as the negative control. The plates were incubated at 37 ºC for 24 h, after which the antibacterial activity was assessed by measuring the diameter of the inhibition zones formed around the wells. All experiments were performed under sterile conditions, and the results were recorded as mean values of inhibition zone diameters.

RESULTS AND DISCUSSION

XRD studies: Fig. 1 presents the X-ray diffraction patterns of the ZnO thin films deposited at different precursor concentrations. The diffraction peaks observed at 2θ values of 31.78º, 34.53º, 36.01º, 47.34º, 57.58º, 64.98º and 67.84º correspond to the (100), (002), (101), (102), (110), (103) and (112) lattice planes, respectively, and are in good agreement with the standard hexagonal wurtzite ZnO phase (JCPDS No. 01-084-6784). Except for the film deposited at 0.3 M concentration, all samples exhibit a preferred orientation along the (101) plane, indicating enhanced crystallographic alignment. The sharp and well-defined diffraction peaks, particularly those associated with the (100) and (101) planes, confirm the good crystalline quality of the films. No additional diffraction peaks corresponding to secondary phases or impurities were detected, indicating the formation of phase-pure ZnO. A gradual variation in the relative peak intensities with increasing precursor concentration suggests that molarity plays a significant role in influencing crystallite orientation and growth behaviour. Using the Debye-Scherrer equation, the average crystalline size (D) of each sample was determined by taking the dominating peak (1 0 1) growth into account.

$$D = \frac{k\lambda}{\beta \cos\theta} \tag{2}$$

where β is full width at half maximum (FWHM) intensity; k (0.9) is the shape factor; λ is the wavelength of X-ray; θ is the Bragg's angle [35]. It is found that the crystallite size increases from 12.47 nm at 0.3 M to a maximum of 24.49 nm at 0.5 M, followed by a decrease to 18.8 nm at 0.6 M, indicating that precursor concentration strongly influences crystal growth and grain coalescence.

Optical properties: The optical absorption behaviour of the ZnO thin films was analyzed using UV-visible spectroscopy, and the optical band gap (E_g) was estimated using the Tauc relation, which correlates the absorption coefficient (α) and photon energy ($h\nu$) [25]. For direct allowed transitions, the relationship between $(\alpha h\nu)^2$ and $h\nu$ was employed, where the optical band gap corresponds to the intercept of the linear

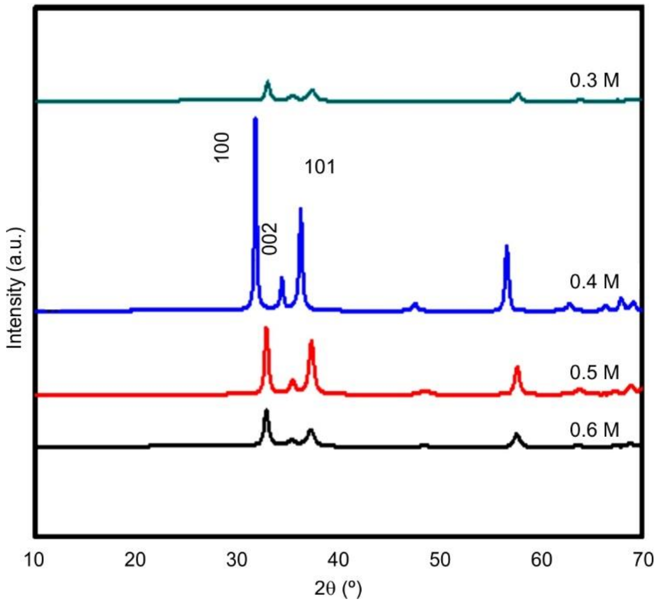

Fig. 1. XRD patterns of the prepared ZnO thin films synthesized various precursor concentrations *viz.* 0.3 M, 0.4 M, 0.5 M and 0.6 M

region with the energy axis. The corresponding Tauc plots for the deposited films are presented in Fig. 2.

The evaluated band gap values for the ZnO thin films were found to vary between 3.02 and 3.44 eV, depending on the precursor concentration. This confirms the strong ultraviolet activity of ZnO [36]. The observed widening of the band gap with increasing concentration can be attributed to the Moss-Burstein effect, which arises from an increase in carrier concentration leading to the filling of lower energy states in the conduction band [37]. In addition, improved crystallinity at higher precursor concentrations contributes to the modulation of the band structure [38]. These band gap values indicate the suitability of the deposited ZnO thin films for applications in gas sensing, solar cells, and photocatalytic systems.

Morphological studies: The surface morphology of the ZnO thin films deposited by ultra-spray pyrolysis was examined using FESEM, and the corresponding micrographs are shown in Fig. 3a-d. The films exhibit nanostructured granular morphology, with noticeable changes as a function of precursor concentration. An increase in molarity from 0.3 M to 0.6 M resulted in the evolution of more compact and uni-

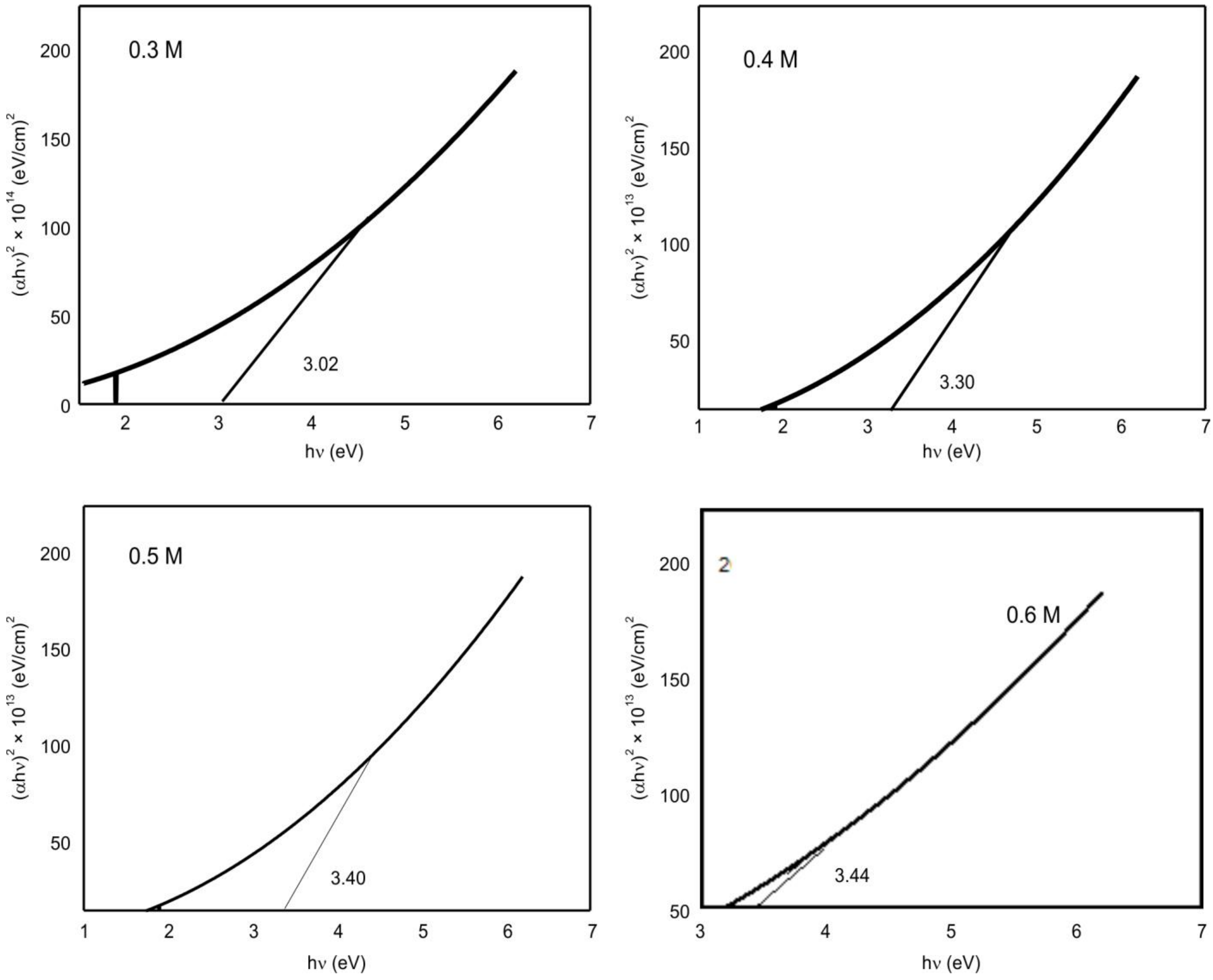

Fig. 2. Plot of $(\alpha h\nu)^2$ *versus* (hν) of samples 0.3 M, 0.4 M, 0.5 M and 0.6 M, respectively

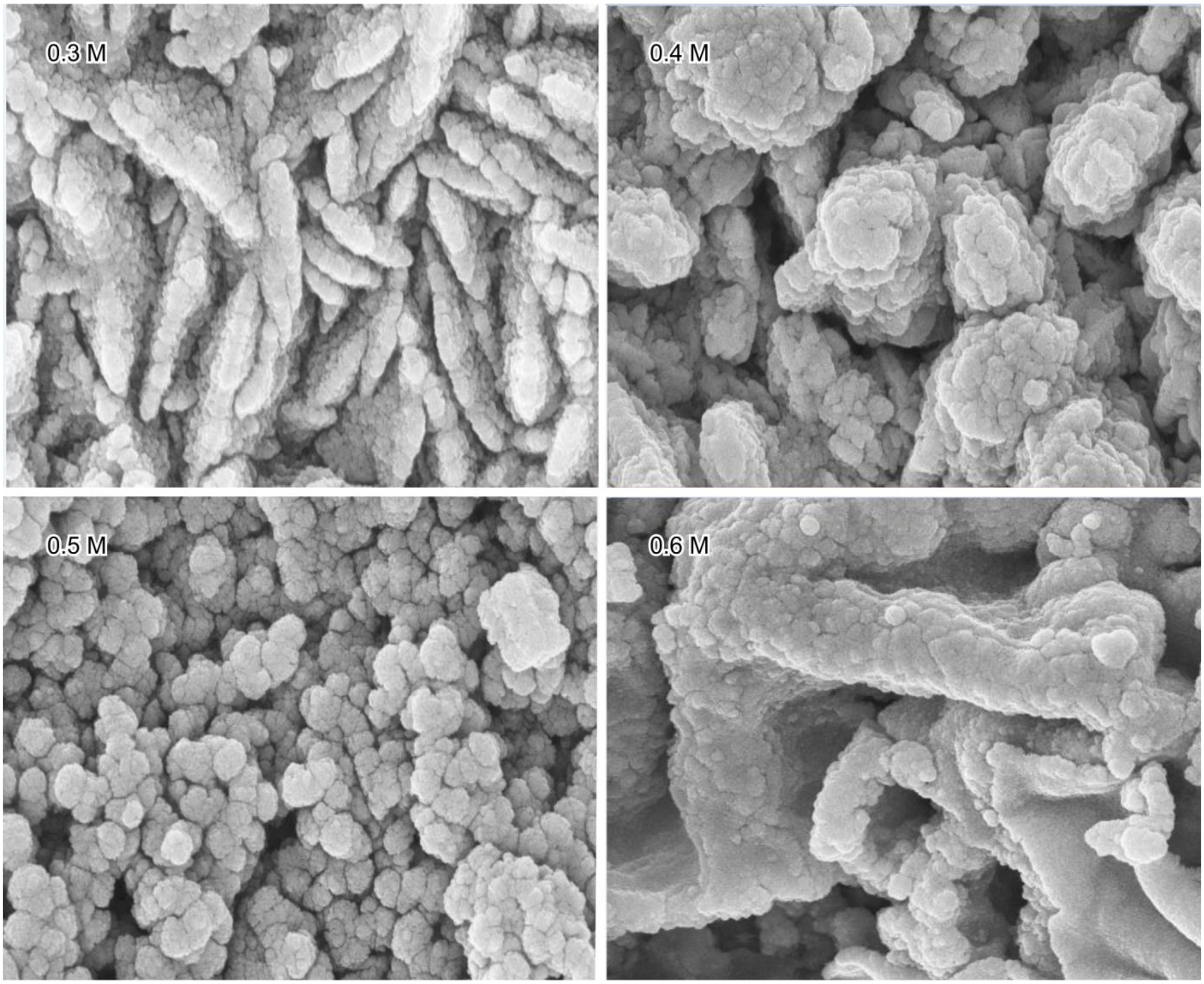

Fig. 3. FESEM images of ZnO thin films of concentrations 0.3 M, 0.4 M, 0.5 M and 0.6 M at different magnifications

form grain structures. Among the samples, the film deposited at 0.5 M displayed relatively well-defined grains and improved surface uniformity, whereas films deposited at 0.3 M and 0.6 M showed less organized nanostructural features. Minor agglomeration was observed for the 0.4 M film, likely due to imperfect grain coalescence during growth.

Energy-dispersive X-ray analysis (EDX), presented in Fig. 4a-d, confirms the presence of only zinc and oxygen elements in all samples, indicating the absence of any kind of impurities. The compositional analysis suggests oxygen-rich stoichiometry, which is known to influence defect chemistry and functional properties of ZnO thin films.

X-ray photoelectron spectroscopy (XPS): The XPS spectrum (Fig. 5a) confirms the presence of Zn and O without any detectable contamination, verifying the chemical purity of the films. Binding energy calibration was carried out using the C 1s reference peak at 284.38 eV. High-resolution Zn 2p spectra (Fig. 5b) exhibit characteristic peaks at binding energies of approximately 1020.97 eV (Zn $2p_{3/2}$) and 1044.44 eV (Zn $2p_{1/2}$), corresponding to Zn in the divalent oxidation state (Zn^{2+}), which is typical of wurtzite ZnO [39]. The energy separation of 23.47 eV between these peaks further confirms the formation of ZnO [40].

To gain deeper insight into the chemical environment of zinc, Zn LMM Auger spectra were analyzed (Fig. 5c). The observed Auger peak at approximately 529.40 eV is consistent with reported values for ZnO [41,42], indicating oxygen-rich stoichiometry and minimal interstitial zinc defects. The O 1s spectrum was deconvoluted into three components corresponding to lattice oxygen (O_L), oxygen vacancies (V_O) and interstitial oxygen (O_i) [40,41]. The presence of oxygen vacancy related peaks suggests defect states that can significantly influence optical absorption and gas-sensing performance.

Atomic force microscopy (AFM): The AFM images (Fig. 6a-d) reveal grain-like surface features, with grain size decreasing as the precursor concentration increases. This trend results in smoother and more compact film surfaces at higher molarity. The root mean square (RMS) roughness values were determined to be approximately 217 nm for the 0.3 M film and 8.94 nm for 0.5 M film. The significant reduction in surface roughness with increasing concentration indicates enhanced crystallinity and improved surface uniformity [43]. Such

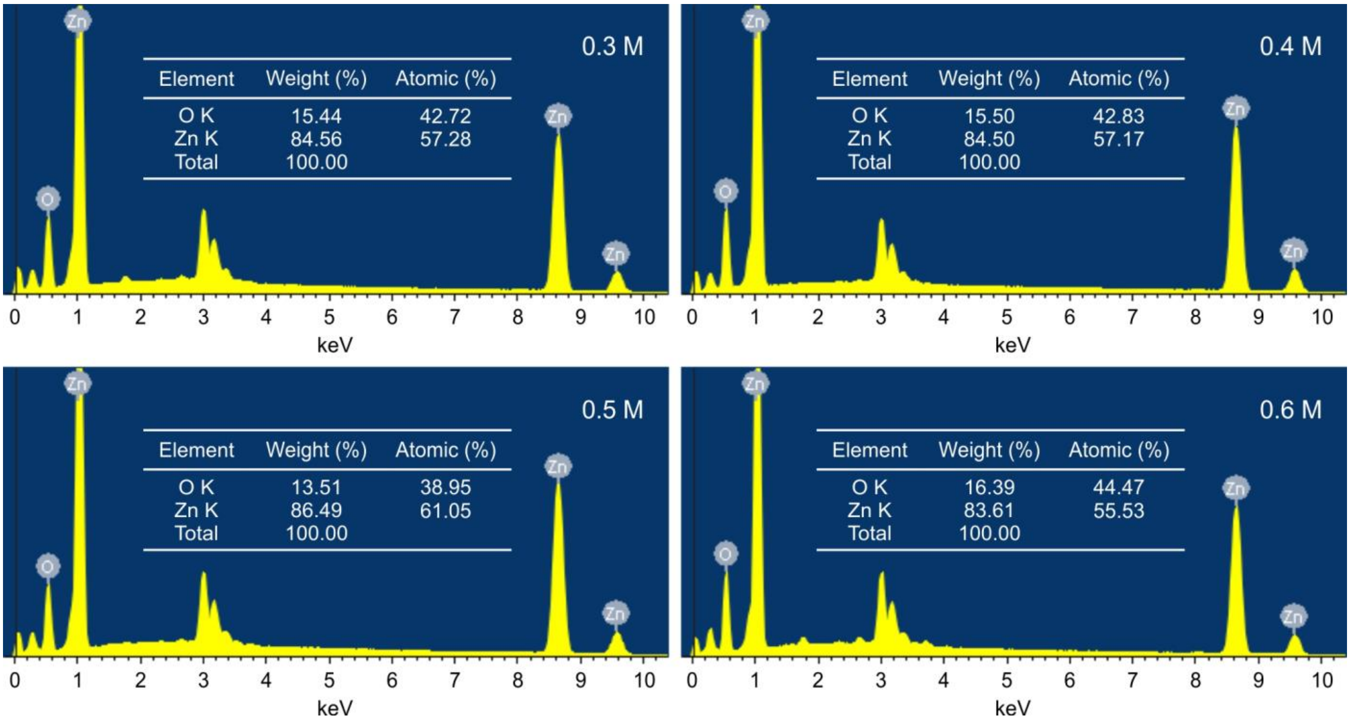

0.3 M

Element	Weight (%)	Atomic (%)
O K	15.44	42.72
Zn K	84.56	57.28
Total	100.00	

0.4 M

Element	Weight (%)	Atomic (%)
O K	15.50	42.83
Zn K	84.50	57.17
Total	100.00	

0.5 M

Element	Weight (%)	Atomic (%)
O K	13.51	38.95
Zn K	86.49	61.05
Total	100.00	

0.6 M

Element	Weight (%)	Atomic (%)
O K	16.39	44.47
Zn K	83.61	55.53
Total	100.00	

Fig. 4. EDAX for ZnO concentrations: (a) 0.3 M (b) 0.4 M (c) 0.5 M and (d) 0.6 M, respectively

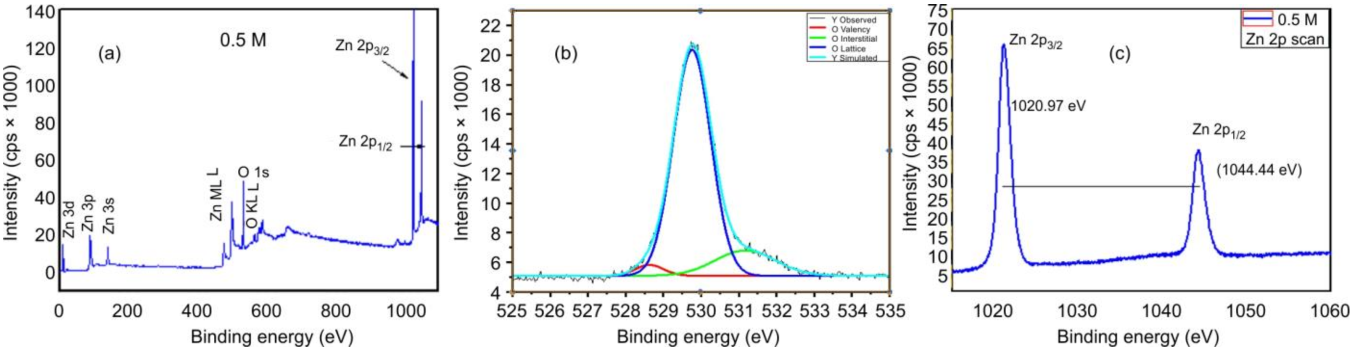

Fig. 5. (a) XPS survey spectrum of ZnO nanoparticles; (b) XPS core level scan of O 1s. Existence of OL, VO and Oi states is shown through deconvoluted profiles and (c) Zn $2p_{1/2}$ and $2p_{3/2}$ core level scans

smooth and dense morphologies are advantageous for applications requiring stable electrical transport and surface-controlled interactions, particularly in gas sensing.

Gas sensing properties: The gas-sensing characteristics of the ZnO thin films were evaluated using a custom-built sensor system consisting of an airtight stainless-steel test chamber. Sensor performance was assessed by monitoring changes in electrical resistance upon exposure to target gases. ZnO thin films with identical actve areas were mounted on a sample holder and placed inside the chamber to ensure consistency across measurements. After introducing a known concentration of test gas into the chamber, the corresponding resistance variation was recorded, and the gas response was calculated using Eq. (1).

$$S = \frac{R_g}{R_a} \qquad (1)$$

where, R_g is the resistance of sensor material in presence of target gas, R_a is the resistance of sensor material in presence of atmospheric gas.

Selectivity is a critical parameter for gas sensor performance. Accordingly, the selectivity of the ZnO thin films was examined against commonly interfering gases, including acetone, LPG, NH_3, SO_2 and NO_2, each at a concentration of 40 ppm under identical conditions. As shown in Fig. 7a, the ZnO thin films exhibited a significantly higher response toward NO_2 compared to other gases, demonstrating good selectivity for NO_2 detection.

The influence of precursor concentrations on NO_2 sensing performance was systematically investigated. Fig. 7b shows the response of 0.6 M ZnO thin film toward 40 ppm NO_2 as a function of operating temperature in the range of 150-200 ºC. The sensor response increased with temperature up to an optimum value of 190 ºC and decreased thereafter. The reduction in sensitivity at higher temperatures can be attributed to the decreased adsorption probability of NO_2 molecules and enhanced desorption kinetics, consistent with Langmuir adsorption behaviour [44]. Moreover, partial conversion of NO_2 to NO at elevated temperatures contributes to reduced sensor response, as NO is less reactive toward ZnO surfaces [39].

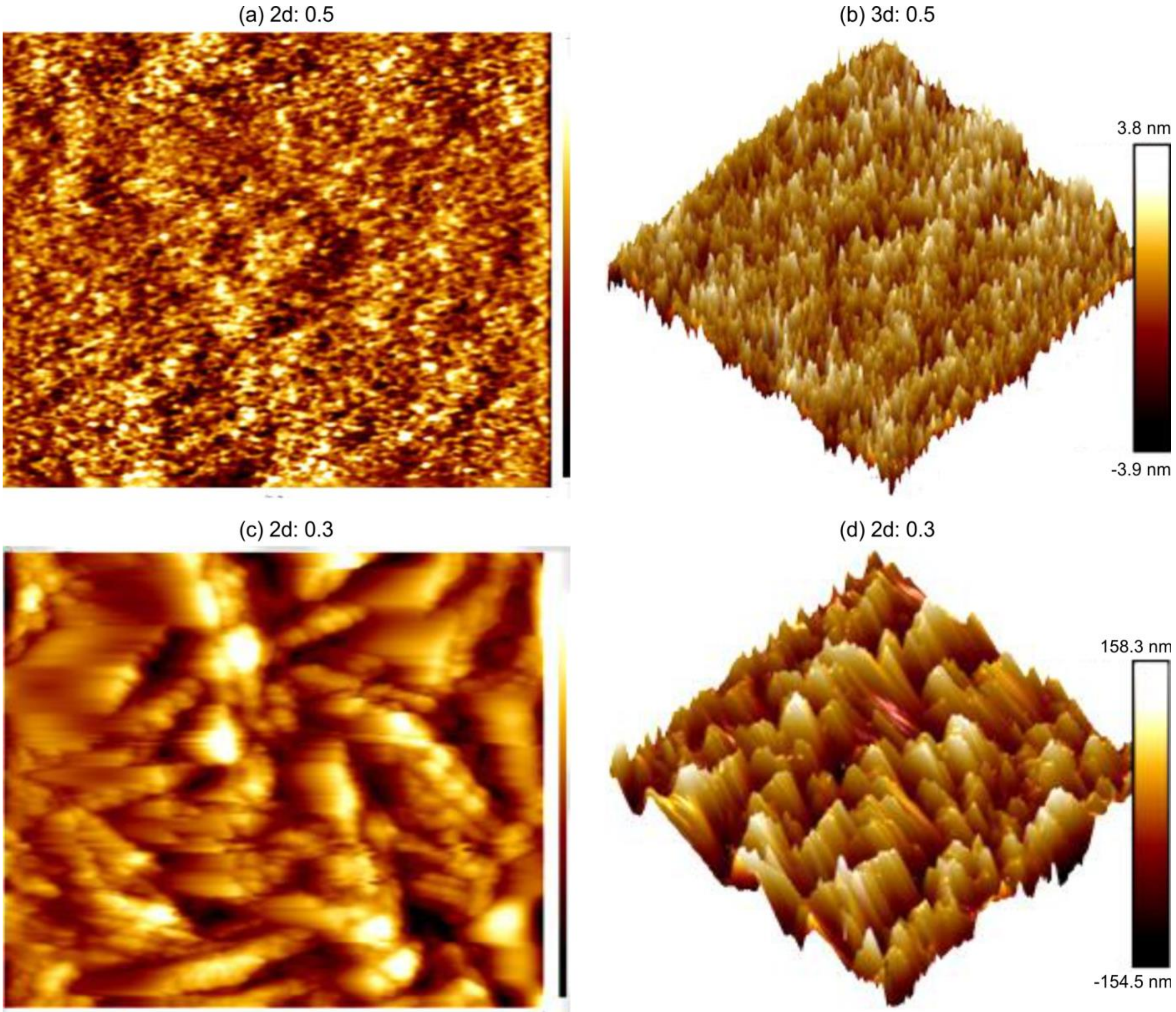

Fig. 6. AFM micrographs in 2D and 3D of ZnO deposited films by zinc acetate tetrahydrate at different molarities and substrate deposition temperature: (a-b) 0.5 M and (c-d) 0.3 M

Dynamic response-recovery characteristics of all ZnO thin films at 40 ppm NO_2 are shown in Fig. 7c. Among the samples, the film deposited at 0.6 M exhibited the highest response (S = 43.61), whereas the responses for 0.3 M, 0.4 M and 0.5 M films were 0.93, 1.54, and 3.13, respectively. This enhanced performance of the 0.6 M film is attributed to improved surface activity and defect-mediated adsorption, and the obtained response compares favourably with previously reported ZnO-based NO_2 sensors [45-47].

Mechanism: The gas-sensing mechanism of ZnO thin films follows the conventional behaviour of n-type semiconducting metal oxides [48,49]. In ambient air, oxygen molecules adsorb on the ZnO surface and capture free electrons from the conduction band, forming ionized oxygen species (O_2^-, O^-). This process creates a surface depletion layer and increases the baseline resistance of the sensor. At the optimized operating temperature of 190 ºC, O^- species are predominant on the ZnO surface [50].

Upon exposure to oxidising NO_2 gas, NO_2 molecules adsorb on the ZnO surface and further extract electrons from the conduction band either directly or by interacting with pre-adsorbed oxygen ions, leading to the formation of NO_2^- species. This electron withdrawal widens the depletion layer and results in a pronounced increase in electrical resistance, as described by eqns. 7 and 8 [51]. According to Debnath *et al.* [50], enhanced sensor response in the temperature range of 150-200 ºC is primarily associated with the dominance of O^- species, whereas higher temperatures favour O^{2-} formation and rapid desorption, leading to reduced sensitivity.

$$NO_{2(g)} + e^- \rightarrow NO^-_{2(ad)} \qquad (7)$$

$$NO^-_{2(ad)} + O^-_{(ad)} + 2e^- \rightarrow NO_g + 2O^{2-}_{(ad)} \qquad (8)$$

Overall, the gas-sensing performance is governed by surface-controlled chemical reactions, effective surface area, and defect-induced adsorption sites [52]. The superior response

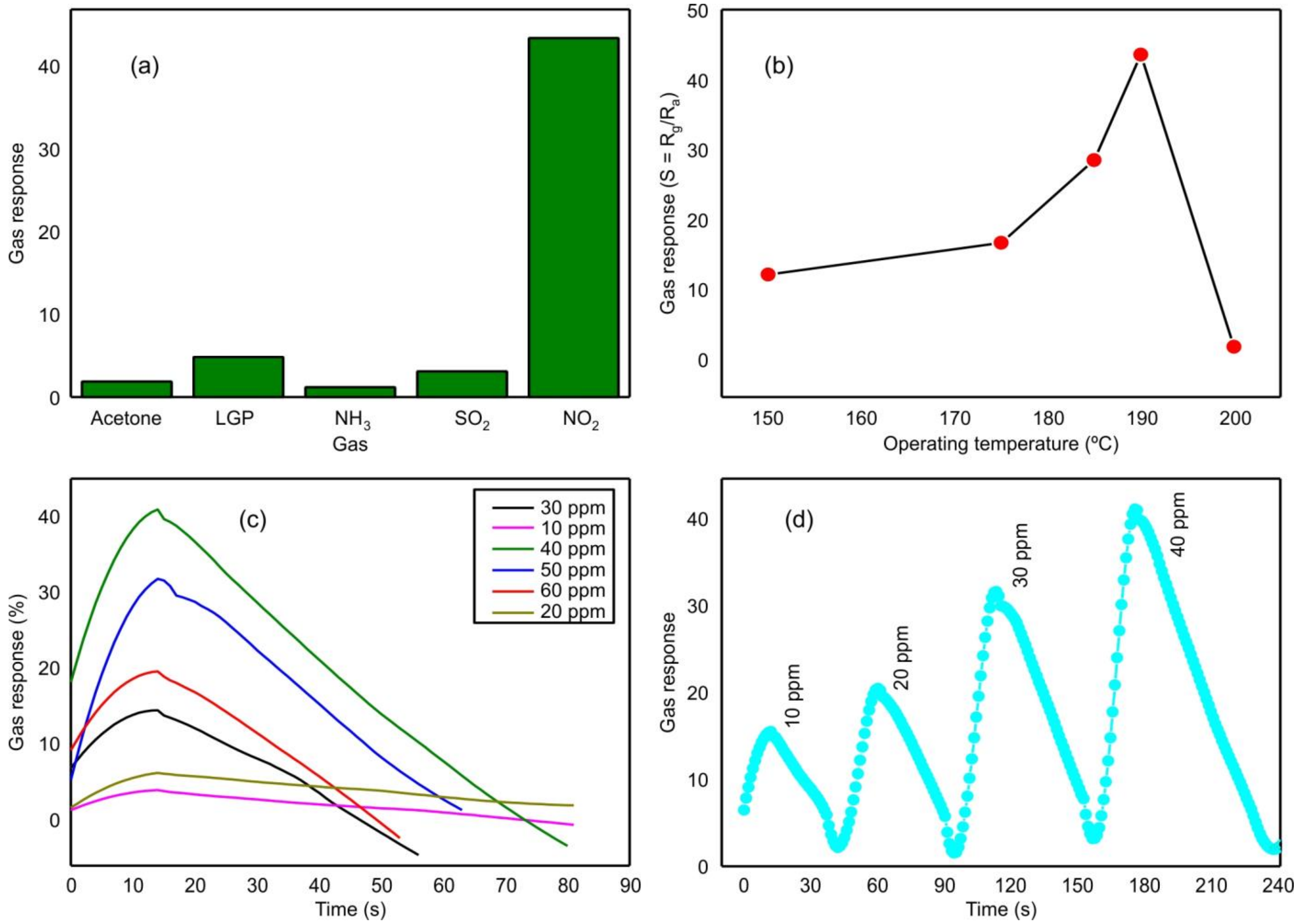

Fig. 7. (a) ZnO thin layer selective for certain gases, (b) gas response as a function of operation temperature, (c) response graph of ZnO thin films to different NO_2 concentrations and (d) gas response curves at different ppm NO_2 for ZnO 0.6 M film

of 0.6 M ZnO thin film (Fig. 7d), confirms that increased precursor concentration enhances surface reactivity and optimizes charge-transfer processes, making it highly suitable for sensitive and selective NO_2 detection.

Antimicrobial activity: The antibacterial activity of ZnO thin films synthesized by the ultra-spray pyrolysis technique was evaluated using the agar-well diffusion method, and the results are summarized in Table-1. The inhibitory effects of the films against *S. aureus*, *E. coli*, *P. aeruginosa* and *B. subtilis* were assessed in comparison with the standard antibiotic streptomycin. All ZnO samples prepared at different precursor concentrations (0.3 M, 0.4 M, 0.5 M and 0.6 M) exhibited low to moderate antibacterial activity.

The antibacterial behavior of ZnO thin films is attributed to their wide band gap (~3.3 eV), which enables the generation of electron-hole pairs under thermal or photoactivation. The photogenerated holes possess strong oxidative potential, leading to the formation of reactive oxygen species (ROS) that initiate oxidative stress and disrupt essential cellular functions. In addition, the release of Zn^{2+} ions from the ZnO surface contributes to the bactericidal effect by interacting with thiol-containing biomolecules, interfering with nutrient transport across the cell membrane, and inducing structural damage to the negatively charged bacterial cell wall. These combined processes ultimately result in bacterial cell death [53,54].

TABLE-1
ANTIBACTERIAL ACTIVITY AGAINST BACTERIA IN TERMS OF ZONE OF INHIBITION (mm)

Sample	Zone of inhibition (mm)			
	E. coli	*P. aeruginosa*	*B. subtilis*	*S. aureus*
0.3 ZnO	15 ± 0.03	14 ± 0.02	05 ± 0.02	18 ± 0.03
0.4 ZnO	19 ± 0.02	18 ± 0.02	13 ± 0.03	16 ± 0.02
0.5 ZnO	17 ± 0.01	16 ± 0.01	05 ± 0.01	15 ± 0.01
0.6 ZnO	14 ± 0.02	16 ± 0.01	07 ± 0.02	15 ± 0.02
Std. streptomycin	26 ± 0.01	25 ± 0.02	19 ± 0.01	23 ± 0.01
Control (DMSO)	00	00	00	00

Among the investigated samples, the ZnO thin film deposited at 0.4 M concentration exhibited the highest antibacterial activity against all tested strains. This enhanced performance is attributed to favourable size and morphological characteristics that promote increased surface reactivity and more efficient interaction with bacterial cells. In contrast, the films deposited at lower (0.3 M) and higher (0.5 M and 0.6 M) concentrations showed comparatively reduced antibacterial efficiency likely due to variations in surface area, grain size and defect distribution.

Conclusion

ZnO thin films were successfully synthesized by ultra-spray pyrolysis and their properties were found to be strongly dependent on precursor concentration. Structural analysis confirmed phase-pure wurtzite ZnO with concentration variations in crystallite size and orientation. Optical studies revealed tunable band gaps (3.02-3.44 eV), while morphological and surface analyses showed smoother, denser films at higher molarities with beneficial oxygen-related defects. Gas-sensing measurements demonstrated high selectivity toward NO_2, with the 0.6 M film exhibiting the highest response (S = 43.61) at 190 ºC due to enhanced surface reactivity and defect-assisted charge transfer. The films also displayed antibacterial activity against both Gram-positive and Gram-negative bacteria, with 0.4 M sample showing superior performance attributed to favourable surface characteristics. These results highlight ultra-spray pyrolysis as an effective route for fabricating multifunctional ZnO thin films for gas-sensing and antimicrobial applications.

CONFLICT OF INTEREST

The authors declare that there is no conflict of interests regarding the publication of this article.

REFERENCES

1. S.P. Patil, V.L. Patil, S.S. Shendage, N.S. Harale, S.A. Vanalakar, J.H. Kim and P.S. Patil, *Ceram. Int.*, **42**, 16160 (2016); https://doi.org/10.1016/j.ceramint.2016.07.135
2. S. Tyagi, M. Chaudhary, A.K. Ambedkar, K. Sharma, Y.K. Gautam and B.P. Singh, *Sens. Diagn.*, **1**, 106 (2022); https://doi.org/10.1039/D1SD00034A
3. Y. Yan, G. Yang, J.-L. Xu, M. Zhang, C.-C. Kuo and S.-D. Wang, *Sci. Technol. Adv. Mater.*, **21**, 768 (2021); https://doi.org/10.1080/14686996.2020.1820845
4. S.S. Shendage, V.L. Patil, S.P. Patil, S.A. Vanalakar, J.L. Bhosale, J.H. Kim and P.S. Patil, *J. Anal. Appl. Pyrolysis*, **125**, 9 (2017); https://doi.org/10.1016/j.jaap.2017.05.006
5. S.R. Bhosale, R.R. Bhosale, D.N. Patil, R.P. Dhavale, G.B. Kolekar, V.B. Shimpale and P.V. Anbhule, *Langmuir*, **39**, 11910 (2023); https://doi.org/10.1021/acs.langmuir.3c01715
6. S.R. Bhosale, R.R. Bhosale, G.S. Kamble, S.S. Shukla, S.R. Gadale, R.P. Dhavale and P.V. Anbhule, *Inorg. Chem. Commun.*, **161**, 112111 (2024); https://doi.org/10.1016/j.inoche.2024.112111
7. S.R. Bhosale, R.R. Bhosale, R.P. Dhavale, G.B. Kolekar, V.B. Shimpale and P.V. Anbhule, *Langmuir*, **40**, 6471 (2024); https://doi.org/10.1021/acs.langmuir.4c00010
8. V. Tsikourkitoudi, B. Henriques-Normark and G.A. Sotiriou, *Curr. Opin. Chem. Eng.*, **38**, 100872 (2022); https://doi.org/10.1016/j.coche.2022.100872
9. J.L. Konne and B.O. Christopher, *J. Nanotechnol.*, **2017**, 1 (2017); https://doi.org/10.1155/2017/5219850
10. T.U. Doan Thi, T.T. Nguyen, Y.D. Thi, K.H. Ta Thi, B.T. Phan and K.N. Pham, *RSC Adv.*, **10**, 23899 (2020); https://doi.org/10.1039/D0RA04926C
11. D. Zhao, S. Sathasivam, M. Wang and C.J. Carmalt, *RSC Adv.*, **12**, 33049 (2022); https://doi.org/10.1039/D2RA05895B
12. R. Maller, Y. Porte, H.N. Alshareef and M.A. McLachlan, *J. Mater. Chem. C Mater. Opt. Electron. Devices*, **4**, 5953 (2016); https://doi.org/10.1039/C5TC03636D
13. G. El Fidha, N. Bitri, F. Chaabouni, S. Acosta, F. Güell, C. Bittencourt, J. Casanova-Chafer and E. Llobet, *RSC Adv.*, **11**, 24917 (2021); https://doi.org/10.1039/D1RA03967A
14. N.B. Mahmood, F.R. Saeed, K.R. Gbashi and U.S. Mahmood, *Mater. Lett. X.*, **13**, 100126 (2022); https://doi.org/10.1016/j.mlblux.2022.100126
15. R.E. Adam, G. Pozina, M. Willander and O. Nur, *Appl.*, **32**, 11 (2018);
16. J. Singh, S. Sharma, S. Soni, S. Sharma and R. Chand Singh, *Mater. Sci. Semicond. Process.*, **98**, 29 (2019); https://doi.org/10.1016/j.mssp.2019.03.026
17. S. Bazazi, N. Arsalani, A. Khataee and A.G. Tabrizi, *J. Ind. Eng. Chem.*, **62**, 265 (2018); https://doi.org/10.1016/j.jiec.2018.01.004
18. N.sB. Moussa, M. Lajnef, N. Jebari, C. Villebasse, F. Bayle, J. Chaste, A. Madouri, R. Chtourou and E. Herth, *RSC Adv.*, **11**, 22723 (2021); https://doi.org/10.1039/D1RA02241E
19. A. Rosset, K. Djessas, V. Goetz, S. Grillo and G. Plantard, *RSC Adv.*, **10**, 25456 (2020); https://doi.org/10.1039/C9RA10131D
20. A. Meng, J. Shao, X. Fan, J. Wang and Z. Li, *RSC Adv.*, **4**, 60300 (2014); https://doi.org/10.1039/C4RA09695A
21. P. Porrawatkul, R. Pimsen, A. Kuyyogsuy, N. Teppaya, A. Noypha, S. Chanthai and P. Nuengmatcha, *RSC Adv.*, **12**, 15008 (2022); https://doi.org/10.1039/D2RA01636B
22. M. Pandey, M. Singh, K. Wasnik, S. Gupta, S. Patra, P.S. Gupta, D. Pareek, N.S.N. Chaitanya, S. Maity, A.B.M. Reddy, R. Tilak and P. Paik, *ACS Omega*, **6**, 31615 (2021); https://doi.org/10.1021/acsomega.1c04139
23. S. Umavathi, S. Mahboob, M. Govindarajan, K.A. Al-Ghanim, Z. Ahmed, P. Virik, N. Al-Mulhm, M. Subash, K. Gopinath and C. Kavitha, *Saudi J. Biol. Sci.*, **28**, 1808 (2021); https://doi.org/10.1016/j.sjbs.2020.12.025
24. A.T. Ravichandran and R. Karthick, *Results Mater*, **5**, 100072 (2020); https://doi.org/10.1016/j.rinma.2020.100072
25. G. Kasi and J. Seo, *Mater. Sci. Eng. C*, **98**, 717 (2019); https://doi.org/10.1016/j.msec.2019.01.035
26. V.L. Patil, S.S. Kumbhar, S.A. Vanalakar, N.L. Tarwal, S.S. Mali, J.H. Kim and P.S. Patil, *New J. Chem.*, **42**, 13573 (2018); https://doi.org/10.1039/C8NJ01242C
27. S.A. Vanalakar, M.G. Gang, V.L. Patil, T.D. Dongale, P.S. Patil and J.H. Kim, *J. Electron. Mater.*, **48**, 589 (2019); https://doi.org/10.1007/s11664-018-6752-1
28. M.S. Krishna, S. Singh, M. Batool, H.M. Fahmy, K. Seku, A.E. Shalan, S. Lanceros-Mendez and M.N. Zafar, *Mater. Adv.*, **4**, 320 (2023); https://doi.org/10.1039/D2MA00878E
29. H. Beitollahi, S. Tajik, F. Garkani Nejad and M. Safaei, *J. Mater. Chem. B Mater. Biol. Med.*, **8**, 5826 (2020); https://doi.org/10.1039/D0TB00569J
30. Z. Weng, Y. Xu, J. Gao and X. Wang, *Biomater. Sci.*, **11**, 76 (2022); https://doi.org/10.1039/D2BM01460B
31. N. Garino, P. Sanvitale, B. Dumontel, M. Laurenti, M. Colilla, I. Izquierdo-Barba, V. Cauda and M. Vallet-Regì, *RSC Adv.*, **9**, 11312 (2019); https://doi.org/10.1039/C8RA10236H
32. A. Wang, W. Quan, H. Zhang, H. Li and S. Yang, *RSC Adv.*, **11**, 20465 (2021); https://doi.org/10.1039/D1RA03158A
33. P. Chhattise, S. Saleh, V. Pandit, S. Arbuj and V. Chabukswar, *Mater. Adv.*, **1**, 2339 (2020); https://doi.org/10.1039/D0MA00403K
34. F. Shamsa, A. Motavalizadehkakhky, R. Zhiani, J. Mehrzad and M.S. Hosseiny, *RSC Adv.*, **11**, 37103 (2021); https://doi.org/10.1039/D1RA07197A
35. A.L. Patterson, *Phys. Rev.*, **56**, 978 (1939); https://doi.org/10.1103/PhysRev.56.978

36. E. Burstein, *Phys. Rev.*, **93**, 632 (1954); https://doi.org/10.1103/PhysRev.93.632
37. F. Fan, Y. Feng, S. Bai, J. Feng, A. Chen and D. Li, *Sens. Actuators B Chem.*, **185**, 377 (2013); https://doi.org/10.1016/j.snb.2013.05.020
38. M.N. Islam, T.B. Ghosh, K.L. Chopra and H.N. Acharya, *Thin Solid Films*, **280**, 20 (1996); https://doi.org/10.1016/0040-6090(95)08239-5
39. S.A. Vanalakar, V.L. Patil, N.S. Harale, S.A. Vhanalakar, M.G. Gang, J.Y. Kim, P.S. Patil and J.H. Kim, *Sens. Actuators B Chem.*, **221**, 1195 (2015); https://doi.org/10.1016/j.snb.2015.07.084
40. S.K. Pandey, S.K. Pandey, C. Mukherjee, P. Mishra, M. Gupta, S.R. Barman, S.W. D'Souza and S. Mukherjee, *J. Mater. Sci. Mater. Electron.*, **24**, 2541 (2013); https://doi.org/10.1007/s10854-013-1130-5
41. F. Hai-Bo, Y. Shao-Yan, Z. Pan-Feng, W. Hong-Yuan, L. Xiang-Lin, J. Chun-Mei, Z. Qin-Sheng, C. Yong-Hai and W. Zhan-Guo, *Chin. Phys. Lett.*, **24**, 2108 (2007); https://doi.org/10.1088/0256-307X/24/7/089
42. U. Ilyas, R.S. Rawat, T.L. Tan, P. Lee, R. Chen, H.D. Sun, L. Fengji and S. Zhang, *J. Appl. Phys.*, **110**, 093522 (2011); https://doi.org/10.1063/1.3660284
43. T.V.K. Karthik, A.G. Hernández, Y. Kudriavtsev, H. Gómez-Pozos, M.G. Ramírez-Cruz, L. Martínez-Ayala and A. Escobosa-Echvarria, *J. Mater. Sci. Mater. Electron.*, **31**, 7470 (2020); https://doi.org/10.1007/s10854-020-02987-7
44. J.G. Cuadra, A.C. Estrada, C. Oliveira, L.A. Abderrahim, S. Porcar, D. Fraga, T. Trindade, M.P. Seabra, J. Labrincha and J.B. Carda, *Ceram. Int.*, **49**, 32779 (2023); https://doi.org/10.1016/j.ceramint.2023.07.246
45. S.B. Jagadale, V.L. Patil, S.A. Vanalakar, P.S. Patil and H.P. Deshmukh, *Ceram. Int.*, **44**, 3333 (2018); https://doi.org/10.1016/j.ceramint.2017.11.116
46. S. Bai, J. Hu, D. Li, R. Luo, A. Chen and C. Liu, *J. Mater. Chem.*, **21**, 12288 (2011); https://doi.org/10.1039/c1jm11302j
47. S. Shaikh, V. Ganbavle, S. Inamdar and K. Rajpure, *RSC Adv.*, **6**, 25641 (2016); https://doi.org/10.1039/C6RA01750A
48. J.-C. Jian, Y.-C. Chang, S.-P. Chang and S.-J. Chang, *ACS Omega*, **9**, 1077 (2024); https://doi.org/10.1021/acsomega.3c07280
49. V.L. Patil, S.A. Vanalakar, P.S. Patil and J.H. Kim, *Sens. Actuators B Chem.*, **239**, 1185 (2017); https://doi.org/10.1016/j.snb.2016.08.130
50. S. Kailasa Ganapathi, *Sens. Actuators B Chem.*, **335**, 129678 (2021); https://doi.org/10.1016/j.snb.2021.129678
51. J. Guo, J. Zhang, M. Zhu, D. Ju, H. Xu and B. Cao, *Sens. Actuators B Chem.*, **199**, 339 (2014); https://doi.org/10.1016/j.snb.2014.04.010
52. R.K. Sonker, S.R. Sabhajeet, S. Singh and B.C. Yadav, *Mater. Lett.*, **152**, 189 (2015); https://doi.org/10.1016/j.matlet.2015.03.112
53. C.R. Mendes, G. Dilarri, C.F. Forsan, V.M.R. Sapata, P.R.M. Lopes, P.B. de Moraes, R.N. Montagnolli, H. Ferreira and E.D. Bidoia, *Sci. Rep.*, **12**, 2658 (2022); https://doi.org/10.1038/s41598-022-06657-y
54. A. Sirelkhatim, S. Mahmud, A. Seeni, N.H M. Kaus, L.C. Ann, S.K.M. Bakhori, H. Hasan and D. Mohamad, *Nanomicro Lett.*, **7**, 219 (2015); https://doi.org/10.1007/s40820-015-0040-x